Turkish Journal of Electrical Engineering & Computer Sciences

http://journals.tubitak.gov.tr/elektrik/

Research Article

Turk J Elec Eng & Comp Sci
(2019) 27: 4702 – 4714

doi:10.3906/elk-1709-141

# Design and control of an LCL-type single-phase grid-connected inverter with inverter current feedback using the phase-delay method

**Fatih EVRAN***
Department of Electrical and Electronics Engineering, Faculty of Engineering, Düzce, Turkey

**Received:** 14.09.2017 • **Accepted/Published Online:** 08.07.2019 • **Final Version:** 26.11.2019

**Abstract:** In this study, a novel single-phase grid-connected microinverter system and its control applications are introduced for solar energy systems. The proposed system consists of two stages to transfer solar power to the grid. In the first stage, an isolated high-gain DC/DC converter is used to increase low solar panel output voltage. In the second stage, an inverter is used to supply a sinusoidal current to the grid. Moreover, a proportional resonant controller is adopted to reduce grid current total harmonic distortions (THDs) and an LCL filter is used to provide better harmonic attenuation. However, the ratio between the sampling frequency $f_s$ and the resonance frequency $f_{res}$ should be greater than 6 in the LCL filter with the inverter current feedback for a stable system. In order to obtain higher phase margins, the sampling frequency should be increased, which increases the inverter switching frequency. The present study shows that $f_s/f_{res}$ can be lower than 6 by placing a phase delay on the inverter current feedback path to guarantee adequate stability margins. The effectiveness and feasibility of the proposed method are confirmed by the experimental test results based on a 300-W laboratory prototype.

**Key words:** Inverter, grid-connected system, proportional resonant controller, solar energy, AC module, LCL filter

## 1. Introduction

Nowadays, the importance of renewable energy sources such as solar, wind, and fuel cells has been increasing with the decrease in traditional energy resources [1]. Solar energy from these energy sources is preferred in grid-connected systems due to its decreasing costs over time. Particularly, the AC module known as a module integrated microinverter has become a future trend for photovoltaic (PV) inverter systems. In this system, each PV module has its own maximum power point tracking (MPPT). Therefore, MPPT efficiency can be high [2]. AC module topologies have been classified as nonisolated [3] and isolated [4–12]. Although a grid frequency transformer can provide galvanic isolation between the grid and the PV panel, it is not preferred due to being heavy and bulky [4]. The AC module is supplied by a low-voltage PV panel. Thus, a high frequency transformer is used to provide both voltage gain and galvanic isolation [5–8]. Inverter topologies with a high frequency transformer can be classified into two major categories. In the first configuration, a DC/DC converter produces a rectified sinusoidal waveform [5,6]. Although the switches in the inverter stage operate at grid frequency, the ripple frequency of the PV panel output voltage is twice the grid frequency. This decreases the MPPT efficiency. By contrast, the second configuration has a DC/DC converter to boost the low PV voltage in the first stage and an inverter to inject sinusoidal current to the grid in the second stage [7,8]. A DC link

*Correspondence: fatihevran@duzce.edu.tr

between the converter and the inverter is used to reject the double-grid frequency power ripple reflected from the grid and so MPPT efficiency can be higher. Furthermore, this configuration has a simple control scheme to meet the grid current regulation requirement.

The inverter is an important interface between the PV panel and the grid. Thus, a filter is required to reduce the pulse width modulation (PWM) switching harmonic attenuation and to meet standards [9]. Compared with an L filter, the LCL filter has a very low inductance requirement and provides better attenuation at lower frequencies [10]. However, the main disadvantage of the LCL filter is a resonance issue causing closed loop system instability. To damp this issue, passive [11] and active damping methods [12–15] have been proposed in the literature. Passive damping is realized by adding a resistor in series or in parallel with components of the filter. However, these added resistors decrease both system efficiency and filter effectiveness. The active damping method damps the resonance by using a digital control algorithm such as weighted-feedback current [12], filter-based [13], the capacitor voltage feedback [14], and virtual resistor method [15]. In the weighted-feedback current, the robustness is closely related to the filter parameters. In addition, other methods cannot reject the grid disturbance to the grid current.

In a digitally controlled PWM inverter using inverter-side current feedback, the resonant poles of the LCL filter can force the stability of the entire system [16]. Therefore, the stability of the LCL filter is dependent on the ratio between $f_s$ and $f_{res}$. In digital control systems, there are two significant delays that affect the stability of the system, namely the computation delay of the digital signal processor (DSP) and the modulation delay of the zero-order hold (ZOH).

A time delay of $1.5T_s$ ($T_s = 1/f_s$ is the sampling period with $f_s$ being the sampling frequency) is considered in the control loop [17]. It has been reported that the ratio between $f_s$ and $f_{res}$ should be higher than 6 [17–19]. It should also be noted that $f_s/f_{res}$ should be high for high-bandwidth control of the current loop. In addition, the classic controllers having finite gain cannot eliminate the steady-state tracking error.

In order to overcome this problem, proportional resonant current controller (PRCC) techniques have been successfully investigated and validated [18,19]. In the present paper, a two-stage inverter will be adopted in terms of the grid current quality and steady-state error of the output voltage. In the first stage, a high-gain DC/DC converter is used to increase low PV panel output voltage. The main features of the DC/DC converter are the continuous input current and electrical insulation. In the second stage, a full-bridge inverter is used to inject a sinusoidal current into the grid. Moreover, an LCL filter is used to provide better harmonic attenuation. By placing a phase delay on the inverter current feedback path, $f_s/f_{res}$ can be lower than 6 even under wide variation in grid inductance. Therefore, higher phase margins can be obtained at lower $f_s/f_{res}$. In addition, the PR current controller is adopted to obtain a low THD.

This paper is organized as follows: Section 2 includes a description of the system. Section 3 presents the system modeling and stability analysis. The design process is given in Section 4. The experimental results are given in Section 5 to verify the adopted method. Conclusions are finally drawn in Section 6.

## 2. Operation principle of the system

Figure 1 depicts the proposed topology. It includes two power stages. In the first stage, a high step-up Z-source DC/DC converter regulating DC link voltage and performing the MPPT is used to boost the low PV voltage to the appropriate value. In the second stage, the full bridge inverter supplies sinusoidal current with a unity power factor to the grid through the LCL filter ($L_1$, $L_2$, and $C$). A sinusoidal PWM control (SPWM) is used

in the inverter stage consisting of power switches $S_1 - S_4$ and their antiparallel diodes. A completely digital approach is applied to control the system shown in Figure 2. To calculate the instantaneous PV power, the PV power variation $\Delta P_{pv}$, the PV voltage variation $\Delta v_{pv}$, the PV voltage $v_{pv}$, and the PV current $i_{pv}$ are sensed. MPPT is an algorithm technique that extracts maximum PV panel power under variable weather conditions. Its output generates $v_{pv}^*$ for the PV voltage regulation. The perturb and observe (P&O) algorithm technique is selected as the MPPT method [20].

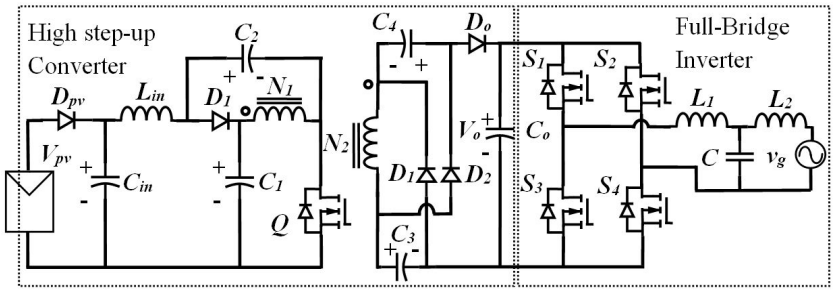


**Figure 1**. Proposed inverter topology.

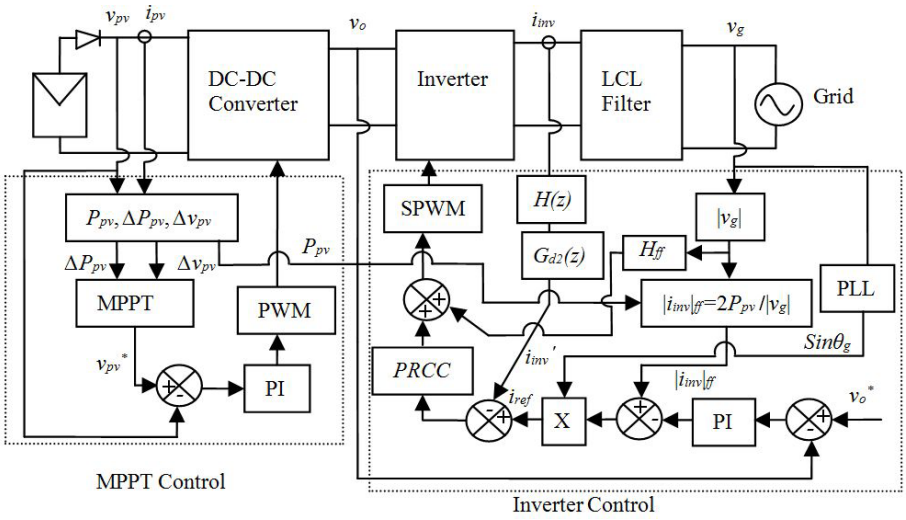


**Figure 2**. Control block diagram of proposed topology.

The instantaneous sinusoidal angle $\theta_g$ extracted by the phase lock loop (PLL) circuit is used to monitor the grid voltage $v_g$ so that the phase and frequency of the grid current can be synchronized with the grid voltage. For the DC-link voltage regulation, the output voltage of the converter ($v_o$) is sensed. The inverter current $i_{inv}$ is sent to the phase delay function via the digital low pass filter. Then the filtered inverter current $i_{inv}^{'}$ is fed back into the PRCC for the inverter current regulation. The grid current and the DC-link voltage references are denoted by $i_{ref}$ and $v_o^*$. A current reference feed-forward is added to achieve fast dynamic responses of the grid current. The magnitude of the current reference feed-forward $|i_{inv}|_{ff}$ and the magnitude of the grid voltage $|v_g|$ are given by

$$|i_{inv}|_{ff} = \frac{2P_{PV}}{|v_g|} \tag{1}$$

$$|v_g| = 0.5 \int_0^{\pi} v_g d\theta_g \tag{2}$$

The practical implementation of a step-up converter is guided by [8] and so the design processes of the converter will not be discussed in the present paper.

## 3. Modeling of an LCL-type inverter with inverter current feedback and stability analysis

Figure 3a shows the continuous time domain model of the LCL-type single-phase grid-connected inverter. $G_c(s)$ is the transfer function of the current controller. $K_{PWM}$ is the PWM gain of the inverter, which can be approximated as $1/V_{tri}$. $V_{tri}$ is the amplitude of the triangle carrier wave and $V_{tri} = 1$. $H_{ff}(s)$ is the admittance compensator to eliminate undesired admittance effect. The inverter can be modeled as a linear $V_o$ gain. The transfer function of the sampler is $1/T_s$. $H(s)$ is a low-pass filter on the feedback path to prevent the switching noises in the sensed inverter current. The modulating signal is $m_a$. The plant function $G_p(s)$ and the disturbance function $G_{dis}(s)$ are given by

$$G_p(s) = \frac{1}{L_1 s} \frac{s^2 + \omega_r^2}{s^2 + \omega_{res}^2}, G_{dis}(s) = \frac{1}{CL_1(L_2 + L_g)s} \cdot \frac{1}{s^2 + \omega_{res}^2}, \tag{3}$$

where the resonance angular frequency $\omega_{res}$ and antiresonance angular frequency $\omega_r$ of the LCL filter can be expressed as follows:

$$\omega_{res} = \sqrt{\frac{L_1 + L_2 + L_g}{L_1(L_2 + L_g)C}}, \omega_r = \sqrt{\frac{1}{(L_2 + L_g)C}}, \tag{4}$$

with $L_g$ being the grid inductance. $G_{d1}(s)$ represents the computation delay, which is one sampling period.

$$G_{d1}(s) = e^{-sT_s} \tag{5}$$

$G_{d2}(s)$ is the phase delay function to guarantee the stability of system, which is expressed as follows:

$$G_{d2}(s) = e^{-snT_s}, \tag{6}$$

where $n$ is the required delay coefficient. The modulation delay with half sampling period is given as

$$G_{zoh}(s) = \frac{1 - e^{-sT_s}}{s} \cong T_s e^{-s0.5T_s} \tag{7}$$

$G_d(s)$ represents the transfer functions of the sampler, the computation delay, and the modulation delay, which is given as

$$G_d(s) = \frac{e^{-sT_s}(1 - e^{-sT_s})}{T_s s} \cong e^{-s1.5T_s} \tag{8}$$

Based on the equivalent model in Figure 3a, the inverter current $i_{inv}$ can be derived as

$$\begin{aligned} i_{inv}(s) &= \frac{1}{G_{d2}(s)H(s)} \cdot \frac{T(s)}{1+T(s)} i_{ref}(s) - \frac{H_{ff}(s)G_d(s)K_{PWM}V_oG_p(s) - G_{dis}(s)}{1+T(s)} v_g(s) \\ &= i_{g1}(s) - i_{g2}(s) \end{aligned} \tag{9}$$

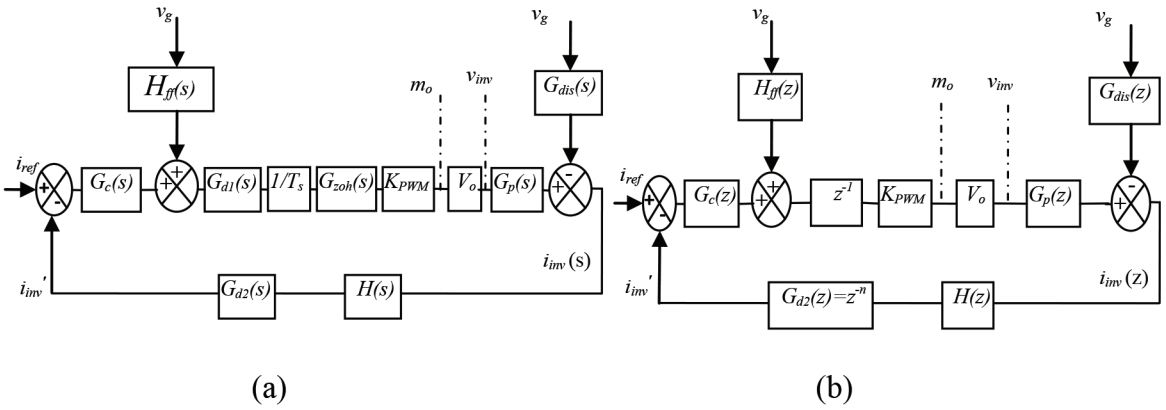


**Figure 3**. Control diagrams: (a) in s-domain, (b) in z-domain.

Here the open-loop function $T(s)$ can be expressed as

$$T(s) = G_{d2}(s)H(s)G_c(s)G_d(s)K_{PWM}V_oG_p(s) = e^{-(1.5+n)sT_s}H(s)G_c(s)K_{PWM}V_oG_p(s) \tag{10}$$

The equivalent series resistors (ESRs) are omitted to obtain the worst case. Eq. (11) shows that the currents $i_{g1}$ and $i_{g2}$ are dependent on $i_{ref}$ and $v_g$, respectively.

$$\begin{aligned} i_{g1}(s) &= \frac{1}{G_{d2}(s)H(s)} \cdot \frac{T(s)}{1+T(s)} i_{ref}(s) \\ i_{g2}(s) &= \frac{H_{ff}(s)G_d(s)K_{PWM}V_oG_p(s) - G_{dis}(s)}{1+T(s)} v_g(s) \end{aligned} \tag{11}$$

The control diagram in the z-domain is shown in Figure 3b. For the digital implementation, the ZOH equivalent of $G_p(s)$ will be

$$\begin{aligned} G_p(z) &= (1-z^{-1})Z\left\{L^{-1}\left[\frac{G_p(s)}{s}\right]\right\} \\ &= (1-z^{-1})Z\left\{L^{-1}\left[\frac{1}{L_1 s^2} \cdot \frac{s^2+\omega_r^2}{s^2+\omega_{res}^2}\right]\right\} \\ &= (1-z^{-1})Z\left\{L^{-1}\left[\frac{1}{L_t s^2} + \frac{L_t - L_1}{L_1 L_t \omega_{res}} \cdot \frac{\omega_{res}}{s^2+\omega_{res}^2}\right]\right\} \\ &= (1-z^{-1})Z\left\{\frac{t}{L_t} + \frac{L_t - L_1}{L_1 L_t} \cdot \frac{\sin(\omega_{res}t)}{\omega_{res}}\right\} \\ &= (1-z^{-1})Z\left\{\frac{T_s z}{L_t(z-1)^2} + \frac{L_t - L_1}{L_1 L_t \omega_{res}} \cdot \frac{\sin(\omega_{res}T_s)z}{z^2 - 2z\cos(\omega_{res}T)+1}\right\} \\ &= \frac{T_s}{L_t(z-1)} + \frac{(L_t - L_1)\sin(\omega_{res}T_s)}{L_1 L_t \omega_{res}} \cdot \frac{z-1}{z^2 - 2z\cos(\omega_{res}T)+1} \end{aligned} \tag{12}$$

where $L_t$ is the total inductance formed by the inductances $L_1$, $L_2$, and $L_g$. With the proportional gain $k_p$ and the resonance gain $k_i$, the PR current controller $G_c(s)$ defined in (13) is adjusted to three times the grid angular frequency $\omega_o$ since the magnitudes of $T(s)$ at fundamental and 3rd harmonic frequencies minimize the steady-state tracking error more than they do at other harmonic frequencies.

$$G_c(s) = k_p + k_i \cdot \frac{s}{s^2 + s + \omega_o^2} + k_i \cdot \frac{s}{s^2 + s + 9\omega_o^2} \tag{13}$$

By applying the prewarped bilinear (Tustin) transformation to (13), $G_c(z)$ is given by

$$G_c(z) = k_p + k_i \cdot A \cdot \left(\frac{z^2-1}{z^2(1+A)-2z\cos(\omega_{res}T)+1-A} + \frac{z^2-1}{z^2(1+8B+A)-2z(1-10B)+1+8B-A}\right),$$
$$A = \frac{\sin(\omega_o T_s)}{2\omega_o}, B = \sin^2(\omega_o T_s/2) \tag{14}$$

Moreover, the digital low-pass filter $H(z)$ with the cutoff frequency of 5.0 kHz is given by

$$H(z) = \frac{(z+1)}{2z} = e^{-j\omega T_s/2}\cos(\omega T_s/2) \tag{15}$$

Based on the control diagram in Figure 3b, the open-loop function in the z-domain can be established as

$$\begin{aligned} T(z) &= z^{-(n+1)}H(z)G_c(z)K_{PWM}V_oG_p(z) \\ &= z^{-(n+1)}H(z)G_c(z)K_{PWM}V_o\left(\frac{T_s}{L_t(z-1)} + \frac{(L_t-L_1)\sin(\omega_{res}T_s)}{L_1L_t\omega_{res}} \cdot \frac{z-1}{z^2-2z\cos(\omega_{res}T)+1}\right) \end{aligned} \tag{16}$$

If $G_c(z)$ is properly designed, the phase lag caused by $G_c(z)$is ignored at the crossover frequency $\omega_c$. In this case, $G_c(z)$ can be simplified as $k_p$. Thus, substituting $|G_c(z)| \approx k_p$ into (16) leads to

$$T(z) = z^{-(n+1)}H(z)k_pK_{PWM}V_o\left(\frac{T_s}{L_t(z-1)} + \frac{(L_t-L_1)\sin(\omega_{res}T_s)}{L_1L_t\omega_{res}} \cdot \frac{z-1}{z^2-2z\cos(\omega_{res}T)+1}\right) \tag{17}$$

The Bode plot and Nyquist stability criterion will be examined for the stability of the open-loop system. In the Bode diagram of $T(z)$, in the frequency ranges where the gain is greater than 0 dB, the phase curve that crosses $\pm$ *(2k + 1)*$\pi$ (k is an integer) is divided into two classes as positive crossing and negative crossing. The crossing of the phase curve from down to up is called the positive crossing, while the crossing of the phase curve from up to down is called the negative crossing. According to the Nyquist stability criterion, the system is stable when $P$equals $2(N_+ - N_-)$, where $P$ is the number of open-loop unstable poles, $N_+$ is the number of positive crossings, and$N_-$ is the number of negative crossings. As can be seen from (12), (14), and (15), there are no unstable loop gain poles ($P$= 0). Therefore, $N_+ - N_-$ = 0 is required. Figure 4 shows the Bode diagrams of $T(z)$ with several different phase delays for the system parameters given in Table 1 case 1. When $n$= 0, there is a negative –180° crossing at resonance frequency ($f_{res}$) where the gain is above 0 dB. Thus, when $P$= 0, $N_+$ =0, and $N_-$ = 1, the system is unstable. As the time delay of $1.5T_s$ cannot be decreased, the value of $n$ should be increased to stabilize the system. When $n$= 1, there is no negative –180° crossing in the frequency ranges where the gain is above 0 dB. When $n$= 2, there is no negative –180° crossing, which indicates a stable system. If $n$ is too high ($n$= 3), a negative –540° crossing is generated at $f_{res}$. This means that the system is unstable again. This analysis clearly identifies that phase delay of a digital low-pass filter significantly affects system stability. Hence, to avoid $\pm$ *(2k + 1)*$\pi$ crossing at $f_{res}$, the following condition should be satisfied:

$$\begin{aligned} \theta_b &< -\pi \\ \theta_a = \theta_b - \pi &> -3\pi \end{aligned}, \tag{18}$$

where $\theta_b$ and $\theta_a$ are the phases before and after the phase jump at $f_{res}$, respectively. As seen from Figure 4, the phase of the LCL filter is similar to the phase of the series inductance $L_t$ until the resonance frequency [19].

Thus, the open-loop transfer function reduces to

$$T(z) = z^{-(n+1)} H(z) k_p K_{PWM} V_o \frac{T_s}{L_t(z-1)} \tag{19}$$

From (19), the phases $\theta_b$ and $\theta_a$ can be calculated as

$$\begin{aligned} \theta_a &= \angle T(z = e^{j\omega_{res}T_s}) = \angle e^{-j\omega_{res}T_s(n+1)} e^{-j\omega_{res}T_s/2} k_p K_{PWM} V_o \frac{T_s}{L_t(e^{j\omega_{res}T_s}-1)} \\ &= -\frac{\pi}{2} - \frac{\omega_{res}T_s}{2} - \omega_{res}T_s - \frac{\omega_{res}T_s}{2} - n\omega_{res}T_s \\ \theta_b &= \theta_a + \pi = \frac{\pi}{2} - \frac{\omega_{res}T_s}{2} - \omega_{res}T_s - \frac{\omega_{res}T_s}{2} - n\omega_{res}T_s \end{aligned} \tag{20}$$

$\theta_a$ in (20) is composed of $\pi/2$, $\omega_{res}T_s/2$, $\omega_{res}T_s$, $\omega_{res}T_s/2$, and $n\omega_{res}T_s$ phase delays. These phase delays are caused by the filter inductor, the modulation delay, the computation delay, the low-pass filter, and the phase delay function, respectively. Substituting the phases $\theta_b$ and $\theta_a$ in (20) into (18),$n$ falls into the following range:

$$\frac{3f_s}{4f_{res}} - 2 < n < \frac{5f_s}{4f_{res}} - 2 \tag{21}$$

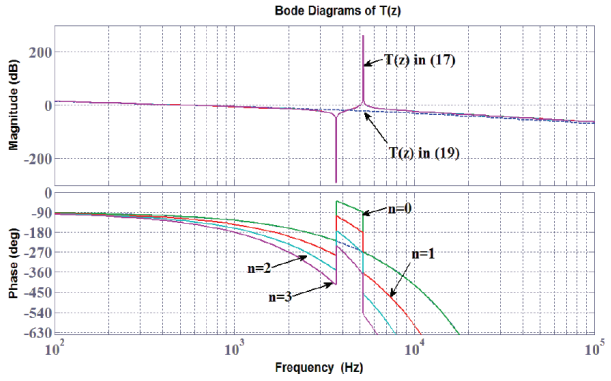


**Figure 4**. Bode diagrams of $T(z)$ with $G_c(z) = kp$ for the different $n$ values.

To investigate the controllability of the system, the closed loop root loci results are shown in Figure 5 for four different $n$ values**.** If $n$ is outside the stability range determined by (21) as shown in Figures 5a and 5d, the system will be unstable since the resonant pole pairs always move outside the unit circle. When $n = 1$, they are very close to the boundary of the unit circle in Figure 5b. However, the instability rises. As seen from Figure 5c, the poles are pushed well inside the unit circle when $n = 2$. Hence, the system is stable depending on the value of $k_p$ and reasonable stability margins can be obtained. Consequently, these root loci outputs match well with the stability condition.

## 4. Design process

### 4.1. Application of the grid admittance compensator

The greater the value of the inverter output impedance $Z_o = v_g(s)/i_{g2}(s)$ in the whole frequency range, the stronger the rejection of grid voltage disturbances [21]. The inverter output impedance tends to be infinitive if

**Table 1**. Component parameters.

| | | |
|---|---|---|
| DC link voltage $V_o$ | 400 V | |
| Inverter switching frequency $f_{sw}$ | 10 kHz | |
| Sampling frequency $f_s$ | 20 kHz | |
| Rated output power $P$ | 300 W | |
| Grid voltage $V_g$ | 120 V | |
| Grid line frequency $f_g$ | 60 Hz | |
| LCL filter design | Case 1 | Case 2 |
| Filter inductance ($L_1$and $L_2$) | 8.5 mH | 8.5 mH |
| Grid inductance $L_g$ | 0 | 0 |
| Filter capacitance $C$ | 220 nF | 1.2 $\mu$F |
| Resonance frequency $f_{res}$ | 5.2 kHz | 2.23 kHz |
| $f_s/f_{res}$ | 3.85 | 8.97 |

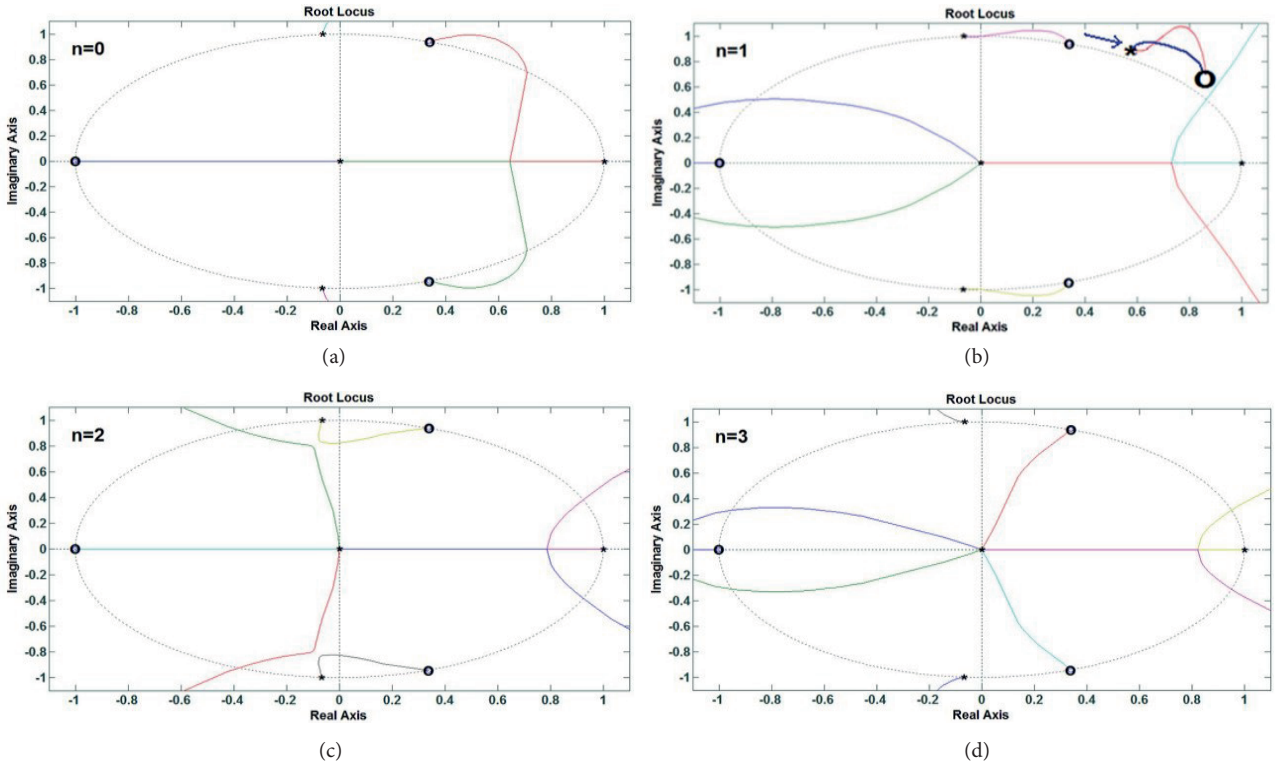


**Figure 5**. Root loci results of $T(z)$. (a) $n=0$, (b) $n=1$, (c) $n=2$, (d) $n=3$.

the compensator transfer function $H_{ff}(s)$ makes the current $i_{g2}$ in (11) zero, which gives

$$H_{ff}(s) = \frac{1}{G_d(s)K_{PWM}V_o} \cdot \frac{1}{s^2(L_2+L_g)C+1} = \frac{e^{s1.5T_s}}{K_{PWM}V_o} \cdot \frac{1}{s^2(L_2+L_g)C+1} \tag{22}$$

Therefore, it is possible to approximate $e^{s1.5Ts} = 1$ and $1/(s^2(L_2+L_g)C) << 1$ because the effect of the transfer functions $e^{s1.5Ts}$ and $1/(s^2(L_2+L_g)C+1)$ on the gain of the compensator transfer function is negligible until the resonance frequency. Thus, by neglecting the second-order differentiator and phase lead blocks in (22), $H_{ff}(s)$ can be simplified as follows:

$$H_{ff}(s) = \frac{1}{K_{PWM}V_o} \tag{23}$$

### 4.2. The selection of $n$

Substituting the parameters given in Table 1 case 1 into (21), $n$ is selected as 2.

### 4.3. The design of the current controller

At the crossover frequency $\omega_c$, the predetermined phase margin $\theta$should be greater than the desired phase margin $\varphi$ because $G_c(z)$ reduces the phase of $T(z)$ by several degrees. Hence, by ignoring the phase reduction caused by $G_c(z)$, $\theta$ can be obtained from (19) as

$$\begin{aligned} \theta &= \pi - \angle T(z = e^{j\omega_c T_s}) = \pi - \tfrac{\pi}{2} - \tfrac{\omega_c T_s}{2} - \omega_c T_s - \tfrac{\omega_c T_s}{2} - n\omega_c T_s \\ \theta &= \tfrac{\pi}{2} - 2\omega_c T_s - n\omega_c T_s \end{aligned} \tag{24}$$

The corresponding crossover frequency $\omega_c$ can be obtained from (24) as

$$\omega_c = \frac{\frac{\pi}{2} - \theta}{(2+n)T_s} \tag{25}$$

For a phase margin of $\theta = 48^\circ$, the crossover frequency $\omega_c$ can be found as 3666 rad/s from (25). At the crossover frequency, open-loop gain is 1, which gives

$$\left|T(z = e^{j\omega_c T_s})\right| = \left| e^{-j\omega_c T_s(n+1)} H(e^{j\omega_c T_s}) k_p K_{PWM} V_o \frac{T_s}{L_t(e^{j\omega_c T_s} - 1)} \right| = 1 \tag{26}$$

Substituting $\omega_c T_s \approx 0.1833$ and the parameters given in Table 1 case 1 into (26), $k_p$ will be

$$\begin{aligned} k_p &= \left| \frac{L_t(e^{j\omega_c T_s} - 1)}{e^{-j\omega_c T_s(n+1)} e^{-j\omega_c T_s/2} \cos(\omega_c T_s/2) K_{PWM} V_o T_s} \right| \\ &= \left| \frac{L_t(e^{j\omega_c T_s} - 1)}{\cos(\omega_c T_s/2) K_{PWM} V_o T_s} \right| = \left| \frac{(L_1+L_2)(Cos\omega_c T_s - 1 + jSin\omega_c T_s)}{\cos(\omega_c T_s/2) K_{PWM} V_o T_s} \right| = 0.1562 \end{aligned} \tag{27}$$

The phase lag caused by $G_c(z)$ at the crossover frequency will be

$$\angle G_c(s) \approx \angle G_c(z) = \angle \begin{bmatrix} k_p + k_i \frac{j\omega_c}{-\omega_c^2 + \omega_o^2 + j\omega_c} \\ \\ +k_i \frac{j\omega_c}{-\omega_c^2 + 9\omega_o^2 + j\omega_c} \end{bmatrix} = \angle \begin{bmatrix} k_p + j\omega_c k_i \cdot \\ \\ \left( \frac{1}{-\omega_c^2 + \omega_o^2} + \frac{1}{-\omega_c^2 + 9\omega_o^2} \right) \end{bmatrix} \tag{28}$$

Finally, $k_i$ can be calculated for $\varphi = 45^\circ$ as

$$k_i = \frac{k_p \tan(\varphi - \theta)}{\omega_c \left( \frac{1}{-\omega_c^2 + \omega_o^2} + \frac{1}{-\omega_c^2 + 9\omega_o^2} \right)} = 14.1834 \tag{29}$$

The final open-loop Bode diagram of $T(z)$is shown in Figure 6. As can be seen from the figure, the measured phase margin is 45.3° and close to the desired one. Thus, the design is appropriate.

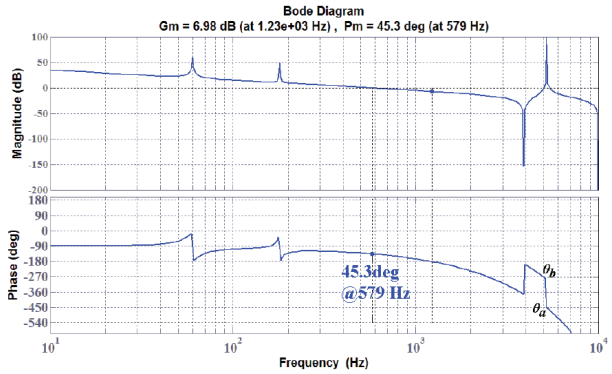


**Figure 6**. Bode diagram of $T(z)$ with PRCC.

## 5. Experimental results

A prototype of 300 W was constructed to verify the proposed the whole system shown in Figure 1. The parameters of the prototype are given in Table 1. The controller employs carrier phase shift sinusoidal pulse-width modulation. The proposed system is implemented using the 32-bit floating point DSP (TMS320F28335). An LG 300N1C PV panel is used as the input power source. A programmable PV panel emulator (Agilent E4350B) is used to realize the PV panel under sudden irradiance changes. Specifications of the PV panel are given in Table 2. In addition, a programmable AC source (Chroma 6590) is used to simulate real-world grid distortion. Using the system parameters given in Table 1 case 1 at full load condition to verify the PR current controller performance, the steady state grid voltage and grid current waveforms are shown in Figure 7, where 3rd, 5th, 7th, 9th, 11th, and 13th harmonics are added to the grid voltage. The amplitudes and phases of the added harmonics are 4%, 4%, 4%, 2%, 2%, and 2% of the grid voltage fundamental amplitude and 0°, 45°, 0°, 0°, 0°, and 0°, respectively. Furthermore, the measured THD of the grid voltage is 7.74%. In Figure 7a, the grid current THD is 11.68% when $H_{ff} = 0$**.** It is clear that the admittance compensator is needed to reduce harmonic distortion of the grid current. As can be seen from Figure 7b, when the admittance compensator is added to the current loop, the current controller ensures that the grid current is perfectly sinusoidal. The measured THD of grid current is 0.87% and the power factor (PF) is 0.993. The waveforms of grid and inverter currents are shown in Figure 8 under step change in load for two different values of $L_g$. As can be seen from the figures, the step change in the grid current reference occurs at the peak value of the grid current reference to indicate the worst case. In Figure 8a, the grid current rapidly follows the grid current reference with small oscillations and the robustness was successfully verified when $L_g = 0$. As seen from Figure 8b, although the increase in $L_g$ reduces the oscillation in the grid current, it causes the transient response to be slower. At full-load condition, the transient waveform is shown in Figure 9a when$n$ jumps from 2 to 3. A trigger signal is used to observe a change in $n$. As can be seen from the figure, the system is stable without resonance for $n=$ 2 before the trigger signal is applied. When$n=$ 3 at the rising edge of the trigger signal, a large resonance current occurs due to the instability of the system. Thus, the inverter is finally shut down after about half a fundamental period. The transient waveform is shown in Figure 9b when the grid current steps from full load to half load. According to Section 4 to achieve a phase margin of 45°, by selecting n = 7 for case 2 in Table 2,

$k_p$ and $k_i$ are set as 0.0693 and 2.8144, respectively. At the rising edge of the trigger signal, $n$ changes from 7 to 0 when the grid current steps from full load to half load. As can be seen from the figure, the oscillation in the grid current implies that the system is slightly stable. To increase the stability of the system, the sampling frequency should be increased or the phase delay function should be added. The experimental results verify the analytical findings. In Figure 10a, the PV panel power drops from 300 to 150 W when the irradiance level changes from 1000 W/m$^2$ to 500 W/m$^2$. It can be seen that the MPPT algorithm tracks the maximum available power of the PV module and the DC-link voltage regulator keeps the bus voltage constant. Finally, the conversion efficiency of the proposed system is summarized in Figure 10b. It is measured for the different PV voltages and a variety of load power levels. When the input voltage is 25 V, the efficiency at full load is 91.6%. The efficiency of 92.3% is achieved at full load when the input voltage is increased to 32 V.

**Table 2**. Specifications of the PV panel.

| | |
|---|---|
| Maximum power $P_{MPP}$ | 300 W |
| MPP voltage $V_{MPP}$ | 32.0 V |
| MPP current $I_{MPP}$ | 9.42 A |
| Open circuit voltage $V_{OC}$ | 39.5 V |
| Short circuit current $I_{SC}$ | 10.0 A |
| Current temperature coefficient $\alpha_{Isc}$ | 0.03%K |

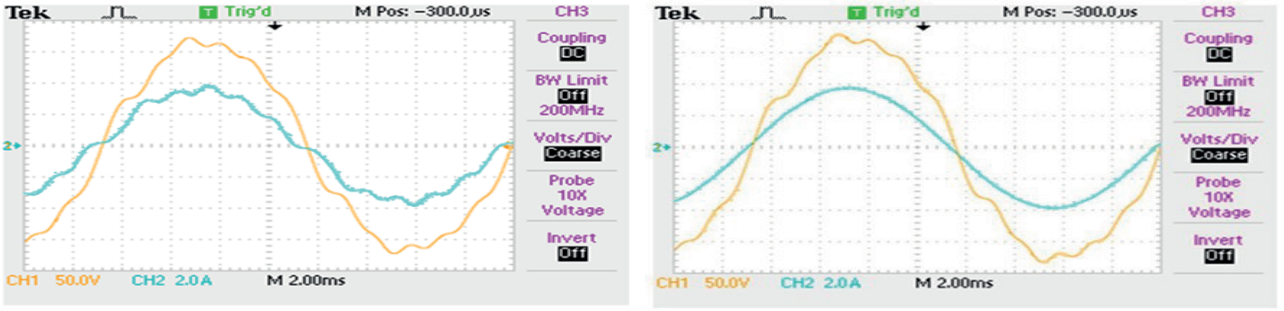


(a) (b)

**Figure 7**. Steady-state waveforms at full load under grid voltage distortion (a) without admittance compensator, (b) with admittance compensator: grid voltage (CH1: [50 V/div]) and grid current (CH2: [2 A/div]).

## 6. Conclusions

In the present study, a novel single-phase grid-connected microinverter system and its control applications are presented for solar energy systems. To improve the stability of an LCL-type single-phase grid-connected inverter with inverter current feedback, the phase delay method is adopted in this paper. The adopted method allows $f_s/f_{res}$ to be lower than 6 even in large grid inductance to obtain higher phase margins. A detailed analysis is then presented for the current controller to obtain a high power factor and minimize current harmonic distortions. Moreover, the adopted system regulates the grid current precisely and stiffly. The experimental results show that the adopted control method not only increases the system stability but also leads to a high power factor ($>0.9$), a reasonably low THD, and fast dynamic response under various load conditions.

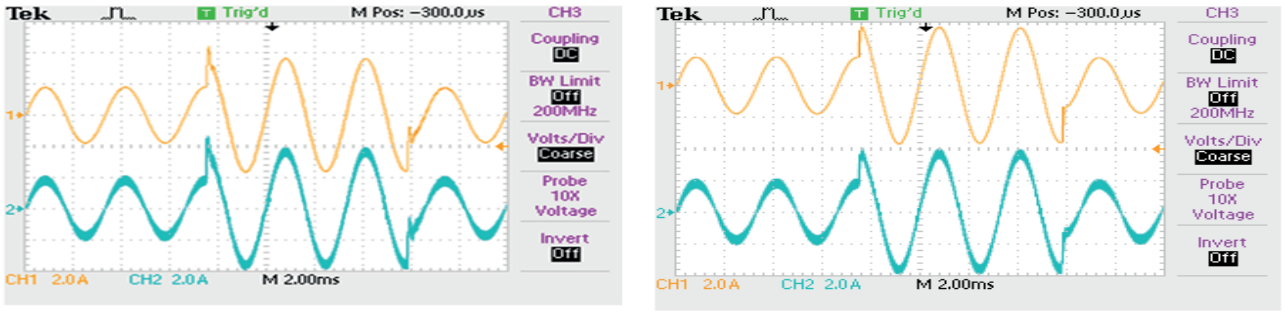


(a) (b)

**Figure 8**. Transient responses under load step change: from top to bottom grid current (CH1: [2 A/div]) and inverter current (CH2: [2 A/div]). (a) $L_g = 0$, (b) $L_g = 10$ mH.

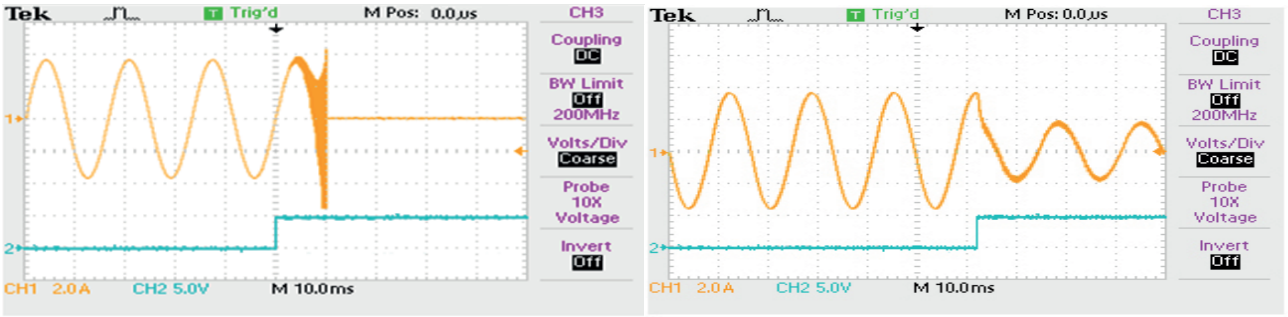


(a) (b)

**Figure 9**. Transient responses (a) when $n$ jumps from 2 to 3, (b) when $n$ steps down from 7 to 0 (grid current (CH1: [2 A/div]) and trigger signal (CH2: [5 V/div])).

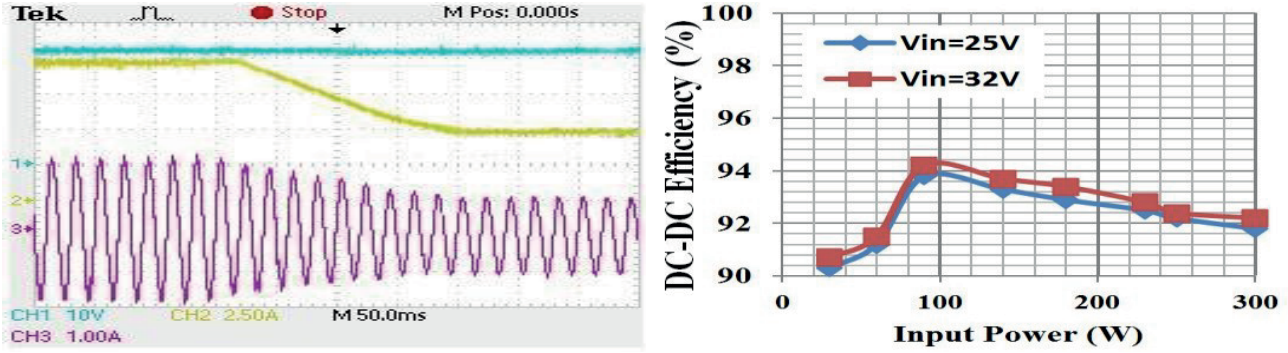


(a) (b)

**Figure 10**. (a) PV voltage (CH1: [10 V/div]), PV current (CH2: [2.5 A/div]), and grid current (CH3: [1 A/div]) under solar irradiance change, (b) conversion efficiency.

## Acknowledgments

This work supported by the Scientific and Technological Research Council of Turkey (TÜBİTAK) was conducted in the Wisconsin Electric Machines and Power Electronics Consortium (WEMPEC) in the Department of

Electrical and Computer Engineering at the University of Wisconsin-Madison in the USA. The author wishes to thank TÜBİTAK for this support.

## References

[1] Liu C, Ge S, Guo Y, Li H, Cai G. Double-LCL resonant compensation network for electric vehicles wireless power transfer: experimental study and analysis. IET Power Electronics 2016; 9: 2262-2270.

[2] Meneses D, Blaabjerg F, Garcia O, Cobos A. Review and comparison of step-up transformerless topologies for photovoltaic AC module application. IEEE Transactions on Power Electronics 2013; 28: 2649-2663.

[3] Cui W, Luo H, Gu Y, Li W, Yang B, He X. Hybrid-bridge transformerless photovoltaic grid-connected inverter. IET Power Electronics 2015; 8: 439-446.

[4] Papanikolaou N, Kyritsis A, Loupis M, Tzotzos C, Zoga E. Design considerations for single-phase line frequency transformers applied at photovoltaic systems. IEEE Power and Energy Technology Systems Journal 2015; 2: 82-93.

[5] Surapaneni RK, Rathore AK. A single-stage CCM zeta microinverter for solar photovoltaic AC module. IEEE Journal of Emerging and Selected Topics in Power Electronics 2015; 3: 892-900.

[6] Rezaei MA, Lee KJ, Huang AQ. A high-efficiency flyback micro-inverter with a new adaptive snubber for photovoltaic applications. IEEE Transactions on Power Electronics 2016; 31: 318-327.

[7] Evran F. Plug-in repetitive control of single-phase grid-connected inverter for AC module applications. IET Power Electronics 2017; 10: 47-58.

[8] Evran F, Aydemir MT. Z-source-based isolated high step-up converter. IET Power Electronics 2013; 6: 117-224.

[9] Liserre M, Blaabjerg F, Hansen S. Design and control of an LCL filter-based three-phase active rectifier. IEEE Transactions on Industry Applications 2005; 41: 1281-1291.

[10] Hoff B, Sulkowski W. Grid-connected VSI with LCL filter-models and comparison. IEEE Transactions on Industry Applications 2014; 50: 1974-1981.

[11] Mukherjee N, De D. Analysis and improvement of performance in LCL filter-based PWM rectifier/inverter application using hybrid damping approach. IET Power Electronics 2013; 6: 309-325.

[12] Shen G, Zhu X, Zhang J, Xu D. A new feedback method for PR current control of LCL-filter-based grid-connected inverter. IEEE Transactions on Industrial Electronics 2010; 57: 2033-2041.

[13] Liserre M, Dell'Aquila A, Blaabjerg F. Genetic algorithm-based design of the active damping for an LCL-filter three-phase active rectifier. IEEE Transactions on Power Electronics 2004; 19: 76-86.

[14] Ghoshal A, John V. Active damping of LCL filter at low switching to resonance frequency ratio. IET Power Electronics 2015; 8: 574-582.

[15] Miskovic V, Blasko V, Jahns TM, Smith AHC, Romenesko C. Observer-based active damping of resonance in grid-connected voltage source converters. IEEE Transactions on Industry Applications 2014; 50: 3977-3985.

[16] Wang J, Yan JD, Jiang L, Zou J. Delay-dependent stability of single-loop controlled grid-connected inverters with LCL filters. IEEE Transactions on Power Electronics 2016; 31: 743-757.

[17] He J, Li YW, Blaabjerg F, Wang X. Active harmonic filtering using current-controlled, grid-connected DG units with closed-loop power control. IEEE Transactions on Power Electronics 2014; 29: 642-653.

[18] Bozorgi AM, Chayjani MS, Nejad RM, Monfared M. Improved grid voltage sensorless control strategy for railway power conditioners. IET Power Electronics 2015; 8: 2454-2461.

[19] Parker SG, McGrath BP, Holmes DG. Regions of active damping control for LCL filters. IEEE Transactions on Industry Applications 2014; 50: 424-432.

[20] Kollimalla SK, Mishra MK. Variable perturbation size adaptive P&O MPPT algorithm for sudden changes in irradiance. IEEE Transactions on Sustainable Energy 2014; 5: 718-728.

[21] Abeyasekera T, Johnson CM, Atkinson DJ, Armstrong M. Suppression of line voltage related distortion in current controlled grid connected inverters. IEEE Transactions on Power Electronics 2005; 20: 1393-1401.